SAND2007-0802C

High-temperature and high-power terahertz quantum-cascade lasers

Benjamin S. Williams[a], Qi Qin[b], Sushil Kumar[b], Qing Hu[b], and John L. Reno[c]

[a]Department of Electrical Engineering, University of California, Los Angeles, California 90095, USA;
[b]Department of Electrical Engineering and Computer Science and Research Laboratory of Electronics, Massachusetts Institute of Technology, Cambridge, Massachusetts 02139, USA;
[c]Sandia National Laboratories, Center for Integrated Nanotechnologies, MS 1303, Albuquerque, New Mexico 87185, USA

ABSTRACT

We summarize recent results in the development of terahertz quantum cascade lasers (QCLs) based on resonant-phonon active region designs. First, we describe attempts to improve high-temperature operation of terahertz QCLs by the use of double-phonon depopulation in order to prevent thermal backfilling of the lower radiative state. While the best of the three tested devices displayed a threshold current density of J_{th}=170 A/cm^2 at 5 K and lased up to 138 K in pulsed mode, no temperature advantage was observed compared to single-phonon designs. Also, we describe high power operation of two different THz QCLs that emit up to 248 mW (pulsed) and 135 mW (continuous-wave) at 4.3–4.5 THz, and 75 mW (pulsed) at 4.8–5.0 THz.

Keywords: terahertz, far-infrared, quantum cascade laser, intersubband laser

1. INTRODUCTION

Since their first demonstration in late 2001, terahertz quantum cascade lasers (QCLs) have been demonstrated as important additions as compact, coherent sources of radiation for the terahertz spectral range (0.3–10 THz), which has historically remained technologically underdeveloped, due in large part to the lack of convenient sources. The terahertz frequency range has been attracting increased interest because of the possibility of applications involving various types of spectroscopy, sensing, and imaging. For example, terahertz radiation shows promise for use in security screening, as many clothing and packaging materials are relatively transparent in this frequency range, and many illicit drugs and explosives have characteristic absorption features there as well. At present, terahertz QCLs now provide continuous-wave (cw) spectral coverage from 1.6–5.0 THz (λ=60–188 μm),[1,2] and as low as 1.36 THz with the assistance of a magnetic field.[3] However, as THz QCLs are currently limited to cryogenic operation (up to 169 K), there is considerable interest in bringing operation to within the range achievable with thermoelectric coolers. Likewise, obtaining higher power lasers is always of interest, particularly for applications involving illumination of many pixels, or transmission through the relatively absorbing atmosphere.

2. TWO-PHONON DEPOPULATION

The best temperature performance for terahertz QCLs has been demonstrated using metal-metal waveguides with the resonant-phonon depopulation scheme, which has allowed operation up to 169 K in pulsed mode and 117 K in cw mode.[4] In this respect terahertz QCLs suffer by comparison with their elder cousins in the mid-infrared (with frequencies above the *reststrahlen* band), for which robust room-temperature cw operation has been demonstrated at wavelengths from 4 to 9 μm.[5,6] It was recognized early in the development of QCLs that thermal backfilling of the lower radiative state by carriers from the heavily populated injector states could effectively lengthen the lower state lifetime τ_l and degrade population inversion; the injector regions were therefore typically designed with large energy separations ($\Delta \geq 100$ meV) between the lower lasing level and the ground state.[7] More recently, mid-IR quantum cascade active regions with doubly resonant longitudinal-optical (LO) phonon depopulation schemes have been used to

demonstrate room-temperature cw operation.[5,6] In this letter, we present results from two QCLs designed for terahertz frequency operation that incorporate similar double-resonant-phonon depopulation schemes.

For terahertz quantum cascade lasers, in addition to thermal backfilling discussed above, we expect an additional process to degrade the intersubband population inversion – which is proportional to the gain – as the temperature increases. For terahertz QCLs, the radiative subband separation $\hbar\omega$ is less than the optical phonon energy E_{LO}. As a result, for electrons that sit in the bottom of the subband, non-radiative relaxation to the lower state via emission of an LO phonon is energetically forbidden. However, during device operation, the electron distribution becomes heated, and electrons acquire sufficient energy to emit LO phonons, so that the upper state lifetime decreases as $\tau_{ul} \propto \exp\left[(\hbar\omega - E_{LO})/k_B T_e\right]$, where T_e is the electronic temperature. Both thermally activated phonon scattering and thermal backfilling sensitively depend on the electron gas temperature T_e, which numerical simulations as well as measurements suggest is 50–100 K higher than the lattice temperature during device operation.[8,9] In a typical terahertz resonant-phonon structure, the injector states are separated from the lower radiative state by approximately $\Delta = E_{LO}$ in order to facilitate fast resonant LO-phonon scattering, as well as to serve as the activation energy barrier against the thermal backfilling process. Therefore, by following the example set by the mid-IR QCLs, one might expect that incorporating a double-phonon depopulation scheme would improve high temperature performance by increasing Δ compared to T_e and by preventing the excitation of carriers from the injector states by reabsorption of nonequilibrium LO phonons (hot-phonon effect).[10]

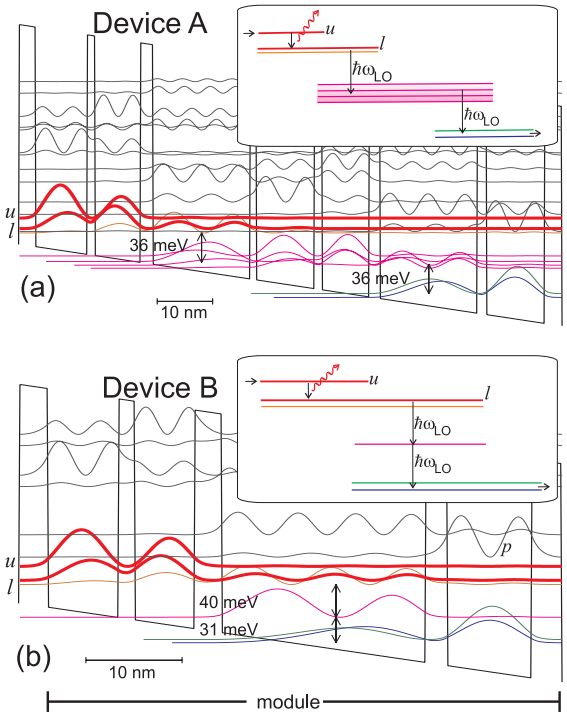

Figure 1. Calculated conduction band diagrams and level schematics for devices A and B. For device A, the layer thicknesses in Å are 31/93/14/82/23/175/11/105/14/85/20/175/17/105, with the underlined layer doped at n=2.8×10^{16} cm^{-3}. For device B, the thicknesses are 31/73/17/62/28/212/23/88, with the underlined layer doped at n=1.4×10^{16} cm^{-3}.

We developed two different implementations of the two-phonon depopulation concept. The conduction band diagrams and energy level schematics for both are shown in Fig. 1, as calculated by using a one-dimensional Schrödinger solver including band nonparabolicity. Both devices were grown by molecular beam epitaxy with GaAs/$Al_{0.3}Ga_{0.7}As$ quantum wells. In both devices, the radiative transition takes place between the upper and lower levels labeled *u* and *l*. For device A (labeled FTP104, wafer EA1126) the two LO-phonon depopulation scattering events are essentially sequential processes and take place in two separate wide wells, which are connected by a four-state miniband with a bandwidth of

approximately 14 meV. Hence the depopulation is through a "phonon-phonon cascade." The thicknesses of the barriers in this miniband were chosen in an attempt to provide fast transport between the wide wells, but thick enough to suppress parasitic coupling between the upper radiative state and any excited states close in energy. In terms of energy level design and applied field (~10 kV/cm at design bias), device A is very similar to a standard resonant phonon structure,[4] except with three extra wells added per module to allow a second phonon depopulation event. Device B (FTP185C, wafer EA1267), on the other hand, is designed to operate at a higher field (~17 kV/cm) and with a single wide well so that both LO-phonon relaxation events take place within a single quantum well. In theory, this "vertical-two-phonon" process should allow a more efficient depopulation, as the resonant tunneling through the miniband in device A may slow the relaxation process. Because of the intrinsic energy level spacings in a single quantum well, it is impossible to design the subband separations in the wide quantum to be exactly equal, but their sum is close to $2\times E_{LO}$. The calculated lower state lifetimes due to LO-phonon scattering are τ_l=0.5 ps for device A and are τ_l=0.35 ps for device B.

Device A was grown with 104 repeated modules and device B with 185 modules to form active regions approximately 10 μm thick. Both devices were grown with cap layers and etch stop layers described in Ref. 4 and were fabricated into metal-metal waveguides using copper-to-copper thermocompression wafer bonding.[4] Laser ridges were cleaved and mounted using indium solder on copper heat sinks on a cold plate in a vacuum cryostat. No facet coatings were used, and power was collected by placing the small aperture of a Winston cone close to one facet and measured by a thermopile detector.

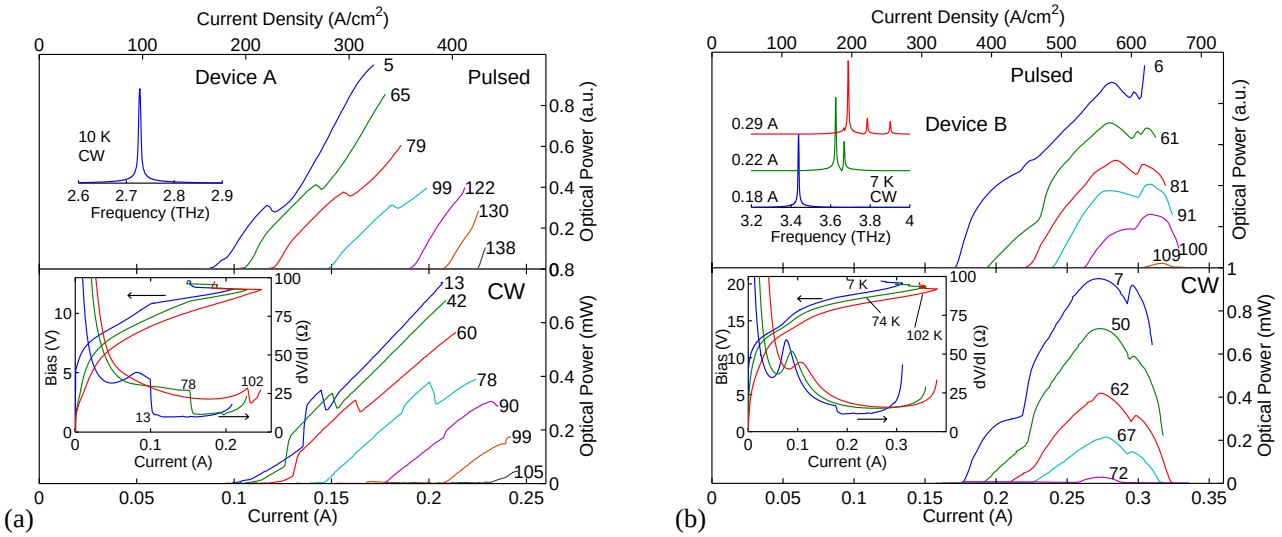

Figure 2. Optical power vs current characteristics for (a) device A with a width of 50 μm and length of 1.06 mm and (b) device B with a width of 40 μm and length of 1.23 mm. Measurements were taken at different heat-sink temperatures with 200 ns pulses repeated at 10 kHz (upper panels) and in cw mode (lower panels). The upper insets display typical cw emission spectra, and the lower insets display cw *V-I* and *dV/ dI-I* characteristics at various heat sink temperatures.

The light versus current (*L-I*) characteristics were collected in both pulsed and cw modes from device A and are plotted in Fig. 2(a). In pulsed mode, the threshold current was J_{th}=170 A/cm^2 at 10 K, and lasing continued up to a maximum temperature of T_{max} = 138 K. Lasing ceases at the maximum current J_{max} when the injection subbands become misaligned, and the device enters into a negative differential resistance (NDR) region. In cw mode, lasing took place at 2.73 THz with J_{th} =185 A/cm^2 at 10 K and a maximum power of 0.75 mW. Two notable features can be seen in the cw voltage versus current (*V-I*) and differential resistance versus current (*dV/dI-I*) characteristics plotted in the inset of Fig. 2(a). First, at 13 K a dip in the differential resistance at 0.05 A reveals the presence of a subthreshold parasitic leakage channel; lasing does not occur until the device is biased beyond this point. Second, at the onset of lasing the clamping of the population inversion is reflected by a sharp kink in the *V-I* curve and a large discontinuity (72% at 13 K) in the

differential resistance. This reflects a large ratio between the upper and lower state lifetimes and indicates highly selective injection and depopulation processes.[11]

Measured *L-I* characteristics and spectra from device B are presented in Fig. 2(b). J_{th} =350 A/cm^2 in pulsed mode and lasing continued up to T_{max}=109 K. At 7 K in cw mode, J_{th} =360 A/cm^2 with a peak power of 0.95 mW, and the device lased at various modes from 3.4 to 3.7 THz. Examination of the *V-I* curve (Fig. 2(b), inset) reveals that the NDR occurs at a relatively high voltage (~20 V) because of the larger designed field for this structure. In this device, the lasing frequency is somewhat higher at 3.4-3.6 THz.

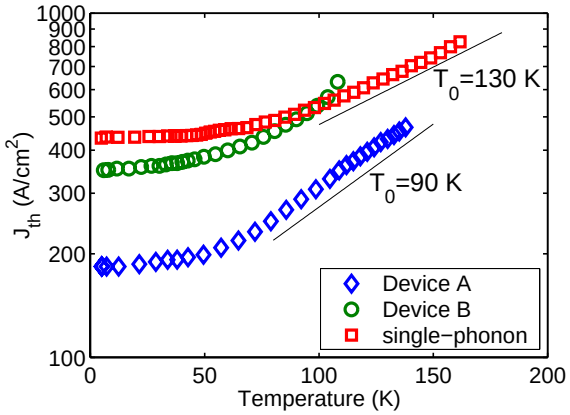

Figure 3. Pulsed threshold current densities vs temperature for device A and B as well as for a 2.9 THz single-resonant-phonon device described in Ref. 4. Fits to the expression $J_{th} \propto \exp(T/T_0)$ are given as guides for the eye.

Unfortunately, no particular improvement is seen in temperature performance for the two double-phonon designs compared to the best performance from single-resonant-phonon designs, which typically lase up to 130–170 K in pulsed mode.[4] In fact, device B exhibits particularly poor temperature performance with T_{max} = 109 K. Indeed, this is contrary to our expectation that a vertical intrawell two-phonon transition would provide a more efficient electron relaxation than device A. The values of J_{th} measured in pulsed mode are plotted versus temperature for both devices in Fig. 3 as well as for the single-resonant-phonon device described in Ref. 4. While all of these lasers have similar dynamic range for lasing current (J_{max}/J_{th} ~ 2), the two-phonon devices degrade more quickly with temperature, i.e., they have smaller characteristic temperatures T_0, where $J_{th} \propto \exp(T/T_0)$ at high temperatures.

For device A, we believe that the faster than typical increase of J_{th} with temperature is due to the strong temperature dependence of the subthreshold parasitic channel. In effect, the low threshold of J_{th} =170 A/cm^2 (compared to J_{th} =300–500 A/cm^2 for previous single-resonant-phonon lasers) may not necessarily be due to intrinsically better depopulation or more gain, but rather a better suppression of parasitic leakage current at low temperatures. This is consistent with the well documented reduction of J_{th} that has accompanied our previous attempts to suppress this parasitic channel.[4,16] If we accept the proposition that J_{th} is limited by this subthreshold leakage current, then the fast increase in the parasitic channel current with temperature (see the *V-I* curve in Fig. 2(a)) would cause a corresponding fast increase in J_{th}. The reason for this dependence likely has to do with the nature of the four-state miniband that couples the two phonon scattering events. At low biases the miniband is not completely aligned, its states are more localized in their respective wells, and transport will be inhibited. At higher temperatures the Fermi distribution of electrons becomes broader and transport through the miniband becomes more efficient, which pushes up the parasitic channel and thus also J_{th}. This mechanism is also likely the cause of the strong increase in J_{max} with temperature (see Fig. 2(a), upper panel), which is somewhat unusual for a resonant-phonon laser.

While device B also suffers from a low T_0 value, this cannot be blamed on a subthreshold leakage channel. Examination of the transport characteristics reveals that the parasitic channel indicated by the minimum in the *dV/dI-I* at *I* ~ 0.05 A barely increases in current between 7 and 74 K, by which point lasing has already ceased. This is because the intrawell two-phonon design has no miniband structure in the middle of the module to selectively impede current flow. However,

there is likely a problem with a different type of parasitic coupling—coupling of the upper radiative state with a higher energy state (labeled "*p*" in Fig. 1(b)). Because of the high field applied to this structure, this state is only 12 meV above the upper radiative state, which is much closer than in a single-phonon structure where this gap is typically 20–30 meV. Thermal excitation of carriers to *p* creates a parasitic current channel and would reduce the upper state lifetime. This is consistent with the roll-off of the *L-I* curve before the NDR, and with the small discontinuity in the *dV/dI-I* characteristic (32% at 7 K) which indicates a smaller lifetime ratio τ_u/τ_l, and is contrary to expectations for this intrawell two-phonon design.

In an attempt to address the issue of the low-lying parasitic energy level present in device B, we developed the modified vertical-two-phonon device shown in Fig. 4, which we will refer to as device C. In this scheme, the wide quantum well was replaced with a tightly coupled triple well, similar to the scheme used for mid-infrared two-phonon QCLs. This scheme gives much more flexibility in designing the lower three energy levels to be separated by E_{LO}, as compared to a single wide well, where the only adjustable parameter is the well width. The trade-off is that the two extremely thin barriers (14 Å and 8 Å) are sensitive to thickness fluctuations, with a resulting uncertainty in the subband energies. This scheme involves the use of narrower wells in general, which pushes all of the states higher in energy, especially the parasitic level *p*, which is now approximately 78 meV higher than the upper state *u* – well out of range for parasitic coupling. Unfortunately, the narrower wells in this structure results in an intrinsically lower dipole matrix element and oscillator strength. In order to counter this effect, the double-well active region was replaced with a 4-well structure in order to increase the oscillator strength up to $f = 0.82$, compared to $f = 0.7$ for device B.

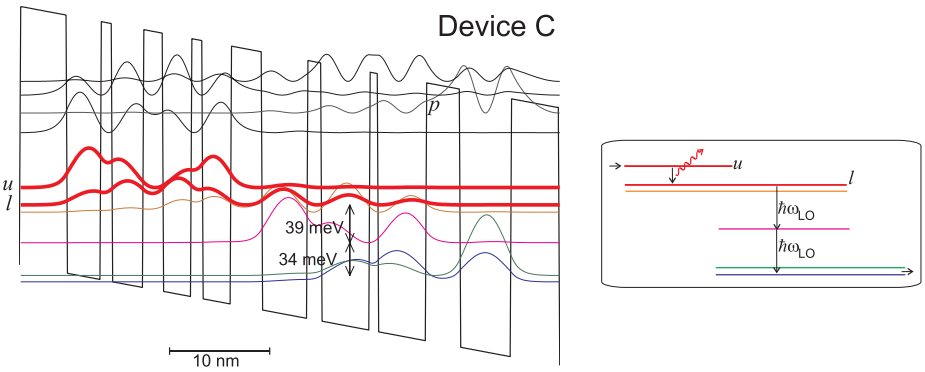

Figure 4. Conduction band diagram and schematic for device C biased at a field of approximately 20 kV/cm. This design is a modified version of a vertical two-phonon depopulation design with the parasitic level p pushed to a much higher energy. The layer thicknesses in Å are 48/34/11/31/20/28/11/28/31/45/14/48/8/48/34/51, with the underlined layers doped at n=2.9×10^{16} cm^{-3}.

Device C (known as FTP160B-M1, or wafer EA1193) was grown with 160 repeated modules (approximately 8 µm-thick active region), and processed in a metal-metal waveguide as described above. A 100 µm-wide, 1.14 mm-long ridge was cleaved from the wafer, and tested in pulsed mode, with the results shown in Fig. 5. Lasing took place at approximately 4.4 THz, which is equivalent to a photon energy of 18.2 meV, close to the calculated value of 18.1 meV. The threshold current density was J_{th} = 614 A/cm^2 at 5 K. Temperature performance was poor, and lasing ceased at T_{max} = 55 K. In continuous-wave mode, no lasing action was observed, presumably because of the high power dissipation from the wide ridge, and the low value of T_{max}. Also, for this device a different In-Au wafer-wafer metallic bonding process was used, which is known to suffer poor heat sinking capability.

Clearly, the modified device C provided no improvement compared to device B, despite the fact that the parasitic level was pushed far away in energy space. The most likely explanation is that far from a simple modification of device B, device C was in fact somewhat of a radical redesign of the vertical two-phonon scheme. In particular, the use of extremely narrow barriers in the wide quantum well of 3 and 5 monolayers is a design where the exact position of the energy levels is very sensitive to the exact thicknesses and heights of the thin barriers. Monolayer growth fluctuations or interface roughness might lead to an uncertainty in the state energies, or lead to inhomogeneously broadened levels, which both of which will degrade performance. While it is true that mid-IR two-phonon QCLs use a similar scheme to

great success, the typical photon energies for mid-IR lasers are a roughly a factor of 10 larger than in the terahertz, and hence are less sensitive to the exact energies. The uncertainties in the energy states might have been compounded by the use of a four-well active region in device C.

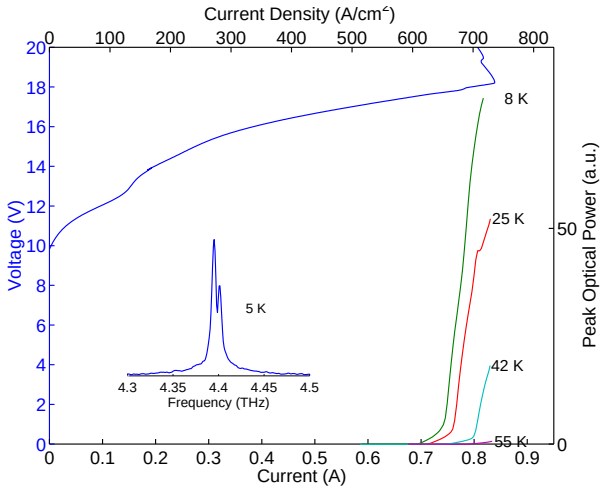

Figure 5. Pulsed *L-I* and *V-I* characteristics for device C with a width of 100 μm and length of 1.14 mm. The inset shows a measured emission spectrum.

In aggregate, these results suggest that for the current generation of resonant-phonon devices, depopulation of the lower state is not yet the limiting factor for performance—at least for the temperatures reached thus far (~170 K). Improvements in depopulation efficiency in the devices reported here appear to have been offset by either a strongly temperature dependent subthreshold leakage channel (device A), a reduced upper state lifetime τ_u due to parasitic coupling with a low-lying excited state (device B). A re-design (device C) that attempted to address the parasitic coupling associated with device B displayed poor performance, likely due to the complexity of the design and accompanying thin barriers. It would appear that in order to develop active regions that operate at higher temperatures, at this time it is more important to focus preserving a long upper state lifetime, rather than thermal backfilling of the lower state. In fact, this is not entirely unexpected, since while τ_u is degraded by thermally activated LO-phonon scattering and τ_l is degraded by thermal backfilling, the activation energy of the former process ($E_{LO} - \hbar\omega$) is smaller than that for the latter ($\Delta \sim E_{LO}$), and so an earlier onset would be expected for the former. However, it should be noted that these designs are merely the first generation of two-phonon designs, and their performance depends on a sensitive interplay of subband alignments; further improvement may be possible by refinement of these designs, as was the case for the single-phonon devices which required many iterations to achieve their current record performance of 169 K.

3. HIGH-POWER THZ QCLS

There is a continuing interest in generating terahertz radiation at higher powers. For example, providing a local oscillator (LO) signal for terahertz heterodyne receivers is a major application for QCLs, and has the potential to replace molecular gas lasers for this purpose, which can provide tens to hundreds of milliwatts of terahertz power at particular frequencies, but are somewhat large and unwieldy and require some effort to maintain their stability. While milliwatt-level LO powers are sufficient to pump single heterodyne mixers, imaging or spectroscopy applications that involve illuminating many pixels, or that require significant material penetration or travel through air would benefit tremendously from much higher power terahertz sources. As mentioned above, the best high-temperature performance has been demonstrated by lasers fabricated using metal-metal waveguides. Because of their subwavelength size in the transverse and lateral dimensions, these waveguides tend to have large facet reflectivities (R~0.7–0.9, depending on the dimensions relative to the wavelength[12]), and low mirror losses α_m, which leads to relatively low output powers (<10 mW), unless steps are taken to prevent the large modal-mismatch between the subwavelength aperture and free space. For this reason, the terahertz QCLs which have displayed the largest peak output powers (~90 mW) have been based on semi-insulating (SI) surface-plasmon waveguides,[13,14,15] which are characterized by a larger transverse mode profile

(confinement factor Γ~0.1–0.5) and do not appear to exhibit enhanced facet reflectivity.[12] As described below, resonant-phonon active regions have been used in conjunction with SI-surface plasmon waveguides to provide high power terahertz QCL operation, up to 248 mW peak power in pulsed operation (138 mW cw) at ~4.4 THz,[15] and up to 70 mW of pulsed power at 4.8 THz.

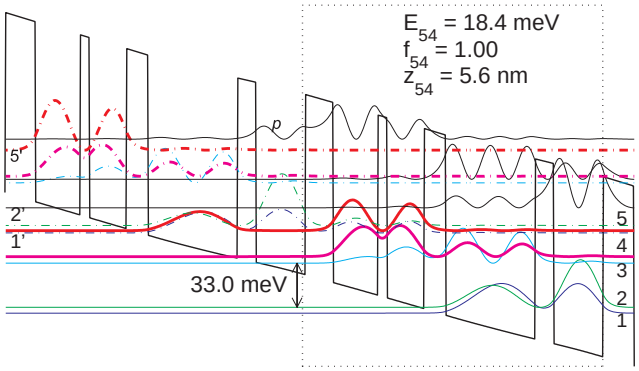

Figure 6. Conduction band diagram for 4.4 THz resonant-phonon active region in GaAs/$Al_{0.15}Ga_{0.85}As$ calculated including nonparabolicity. The layer thicknesses in Å, starting with the injection barrier are 51/82/17/68/40/164/34/90, with the 164 Å well doped to at n=1.9×10^{16} cm^{-3}. The 4.8 THz design was the same, except with the thicknesses 54/82/16/68/42/164/37/90 Å.

Two structures were grown. The first, known as FL183R-2 (EA1229), was composed of 183 repeated modules of the active region shown in Fig. 6. This active region is similar to the 2.9 THz single-phonon resonant device described in Ref. 4, except modified to operate at a larger photon energy, primarily by thinning the radiative barrier from 25 to 17 Å. The wafer was processed into SI-surface-plasmon waveguide ridge structures as described in Ref. 16, with the exception that the heavily doped layer under the active region was 0.4 mm thick and doped at n=3×10^{18} cm^{-3}, and the ridges were dry etched to obtain nearly vertical sidewalls. An undoped 100 nm $Al_{0.55}Ga_{0.45}As$ etch-stop layer was grown underneath the doped contact to allow the option of metal–metal waveguide processing. Finally, the devices were lapped to a substrate thickness of 170 μm, ridges were cleaved, and an Al_2O_3/Ti/Au/Al_2O_3 high-reflectivity (HR) coating was evaporated on the rear facet of selected devices. The mode was calculated using a one-dimensional Drude model solver, which gave a value of α_w=3.9 cm^{-1} for the waveguide loss and a confinement factor of Γ~0.26. A two-dimensional finite-element solver gave similar values of α_w=3.0 cm^{-1} and Γ~0.21 for the fundamental mode in a 200 μm-wide ridge.[12] While the scaled loss (α_w + α_m)/Γ (which determines the threshold) is slightly worse for these waveguides compared to metal-metal waveguides, which typically have Γ~1, the lower absolute value of α_w leads to a more favorable outcoupling ratio α_m /(α_w + α_m), and thus higher slope efficiencies and output powers.

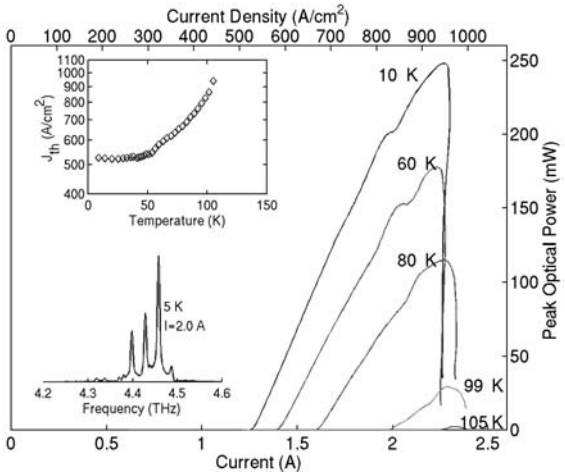

Figure 7. Collected pulsed *L-I* characteristic at various temperatures measured from 198 μm-wide, 1.21 mm-long ridge of the 4.4 THz QCL with a SI-surface-plasmon waveguide and the rear facet HR coated. The upper inset displays the threshold current versus temperature, and the lower inset displays a typical spectrum at a bias current of 2.0 A.

A 198 mm-wide, 1.21 mm-long, HR-coated ridge was mounted in a vacuum cryostat and a Winston cone was used to collect light from the laser facet and bring it to the polypropylene Dewar window. The device was biased with pulse trains of 200 ns pulses repeated at 100 kHz, modulated by a 1 kHz square wave for an overall duty cycle of 1%. The output power was measured with a pyroelectric detector, with the peak level calibrated by a thermopile power meter (ScienTech model AC2500H). The collected peak output power against current is shown in Fig. 7, along with a typical output spectrum. Lasing took place at various frequencies between 4.3 and 4.5 THz, depending on the bias point and temperature of the device. At 5 K, J_{th}=530 A/cm^2 in pulsed mode with a maximum peak power of 248 mW, and lasing was observed up to 105 K. Because of the large power dissipation in this device, the maximum power observed in CW operation was reduced to 138 mW, and lasing ceased at a heat-sink temperature of 35 K. Although J_{th} in these devices is significantly larger than in bound-to-continuum QCLs,[14] these devices also have a large dynamic current range of ~400–500 A/cm^2 above threshold, which results in large output powers. The slope efficiency was measured to be dL/dI = 300 mW/A, or a value of ~340 mW/A after accounting for the 85–90% transmission of the Dewar window. This is equivalent to a differential quantum efficiency (DQE) of approximately 18 photons per injected electron. The DQE is more than a factor of three larger than that observed from the best metal–metal waveguide devices.[4]

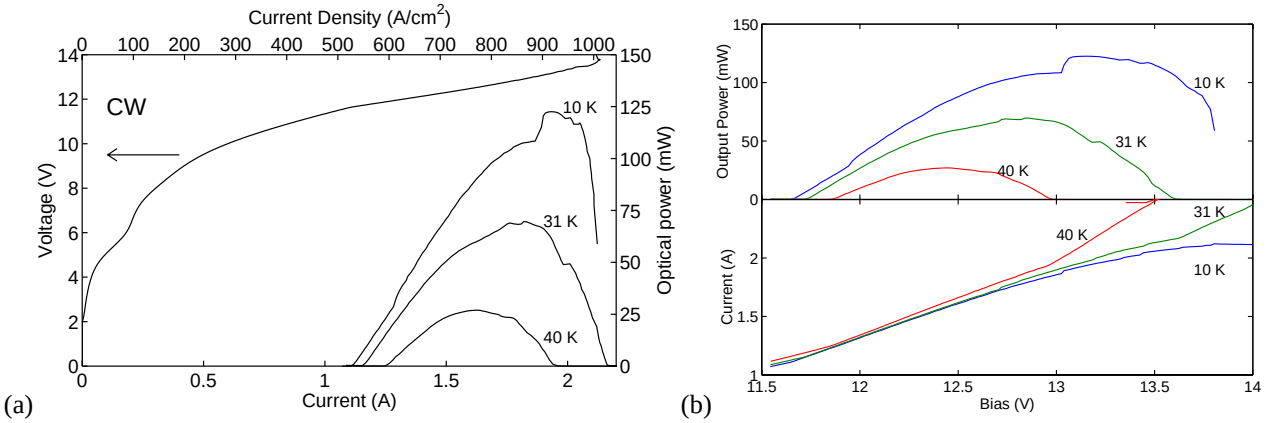

Figure. 8. (a) Continuous wave *L-I* and *V-I* characteristics for a 100 µm-wide, 2.15 mm-long, HR-coated FL183R-2 device. (b) *L-V* and *I-V* characteristics for same device, to highlight the runaway current phenomenon that quenches lasing.

A similar but narrower device (100 µm-wide, 2.15 mm-long, HR-coated) was used to provide up to 125 mW CW power at 10 K more efficiently (wall plug efficiency = 0.5%) due to its reduced thermal dissipation (Fig. 8(a)). Using a closed-cycle pulsed tube cryocooler with a few watts of cooling power at 30 K (Cryomech PT60), this laser still produced ~50 mW of at 30 K, which was used in conjunction with a focal plane array microbolometer camera to perform real-time video-rate terahertz imaging.[17] Careful examination of the cw characteristics also highlights a problem with this design: at high biases and temperatures, the upper radiative state 5' is able to couple with a higher parasitic state *p* (see Fig. 6) which is calculated to be only 8 meV higher in energy at design bias. Transport from 5' into level *p* causes runaway current, which steals population from the upper level and quenches lasing. This can be seen most easily in Fig. 8(b), where the output power and current are plotted versus the voltage bias. The *I-V* characteristic dramatically kinks upward at the same bias where lasing ceases. Furthermore, this occurs at lower biases at higher temperatures. This coupling is difficult to avoid as resonant-phonon lasers are designed at higher-photon energies, due partly to the fact that the upper radiative state must sit at higher energies, and also that the thinner radiative barrier required will also result in the state p sitting at a lower energy.

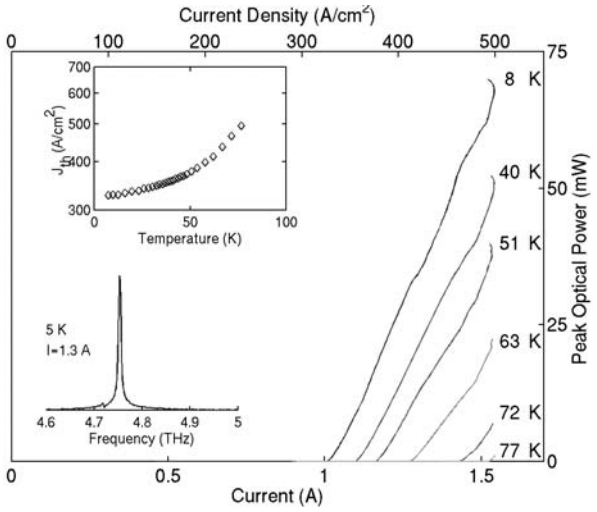

Figure 9. Collected pulsed *L-I* characteristic at various temperatures measured from 150 μm-wide, 2.06 mm-long ridge of the FL179R-M1 device with a SI-surface-plasmon waveguide and the rear facet HR coated. The upper inset displays the threshold current versus temperature, and the lower inset displays a typical spectrum at a bias current of 1.3 A.

A second device, FL179R-M1 (growth EA1320) was grown in an attempt to obtain higher frequency operation, nearer to the 4.7 THz neutral oxygen line (important for monitoring the cooling of interstellar dust), and the atmospheric transmission window at 4.8–4.95 THz. The active region design was the same as that for FL183R-2, but with the radiative barrier narrowed by approximately one-half of a monolayer in order to increase the lasing frequency. Also, the injection barrier, collection barrier, and intra-injection barrier were all increased by one monolayer, in an attempt to suppress the parasitic coupling mechanism exhibited at high-temperatures and high-biases for FL183R-2 and was described above. In fact, this modification did prevent any runaway current phenomenon, but at the cost of reducing the peak current density J_{max} from 1000 A/cm^2 to 500 A/cm^2. The pulsed *L-I* characteristics and a typical spectrum for a 150 μm-wide, 2.06 mm-long ridge is shown in Fig. 9. These devices lased from 4.7–5.0 THz, depending on the bias point and temperature. At 8 K, J_{th} = 327 A/cm^2 and the maximum pulsed power was measured to be 72 mW. The smaller peak power for this device is partially a result of the smaller dynamic range of the device: $(J_{max}-J_{th})/ J_{max} \sim 0.33$, and partially due to the smaller slope efficiency of dL/dI = 130 mW/A. A laser from this wafer was recently used to demonstrate terahertz imaging at 4.9 THz where the radiation propagates over a 25-m distance in an atmospheric transmission window.[18]

While these lasers displayed the highest powers seen to date for terahertz QCLs at these wavelengths, analysis of the slope efficiencies suggest there are still more gains to be made. For example, for the 4.4 THz device, approximately 18/photons per electron are collected. Considering there are 183 stages, this device is still a factor of 10 away from perfect slope efficiency. This is even more true for the 4.8 THz device, where the slope efficiency was even smaller. We believe that we are underestimating the waveguide losses in the SI-surface-plasmon waveguides. This conclusion is bolstered by the fact that when devices from the FL183R-2 wafer were fabricated into metal-metal waveguide ridges (not shown), they exhibited typical thresholds of J_{th} = 327 A/cm^2, which reflects the larger scaled waveguide and mirror losses $(\alpha_w + \alpha_m)/\Gamma$ in the SI-surface-plasmon waveguides. In any case, improvements in waveguiding, output mode coupling, and reduction in lasing thresholds should enable terahertz QCLs with even higher output powers and efficiencies in the future.

ACKNOWLEDGEMENTS

This work is supported by AFOSR, NASA, and NSF. Sandia is a multiprogram laboratory operated by Sandia Corporation, a Lockheed Martin Company, for the United States Department of Energy under Contract DE-AC04-94AL85000.

REFERENCES

1. S. Kumar, B. S. Williams, Q. Qin, Q. Hu, Z. R. Wasilewski, and H. C. Liu, "1.6 THz QCL with one-well injector," (unpublished).
2. C. Walther, G. Scalari, J. Faist, H. Beere, and D. Ritchie, "Low frequency terahertz quantum cascade laser operating from 1.6 to 1.8 THz," Appl. Phys. Lett. **89**, 231121 (2006).
3. G. Scalari, C. Walther, J. Faist, H. Beere, and D. Ritchie," Electrically switchable, two-color quantum cascade laser emitting at 1.39 and 2.3 THz," Appl. Phys. Lett. 88, 141102 (2006).
4. B. S. Williams, S. Kumar, Q. Qin, Q. Hu, and J. L. Reno, "Operation of terahertz quantum-cascade lasers at 164 K in pulsed mode and at 117 K in continuous-wave mode," Opt. Express 13, 3331 (2005).
5. M. Beck, D. Hofstetter, T. Aellen, J. Faist, U. Oesterle, M. Ilegms, E. Gini, and H. Melchior, "Continuous Wave Operation of a Mid-Infrared Semiconductor Laser at Room Temperature," Science 295, 301 (2002).
6. J. S. Yu, S. R. Sarvish, A. Evans, J. Nguyen, S. Slivken, and M. Razeghi, "Room-temperature continuous-wave operation of quantum-cascade lasers at $\lambda \sim 4$ μm," Appl. Phys. Lett. 88, 041111 (2006).
7. C. Sirtori, J. Faist, F. Capasso, D. L. Sivco, A. L. Hutchinson, S. N. G. Chu, and A. Y. Cho, "Continuous wave operation of midinfrared (7.4–8.6 μm) quantum cascade lasers up to 110 K temperature," Appl. Phys. Lett. 68, 1745 (1995).
8. H. Callebaut, S. Kumar, B. S. Williams, Q. Hu, and J. L. Reno, "Importance of electron-impurity scattering for electron transport in terahertz quantum-cascade lasers," Appl. Phys. Lett. 84, 645 (2004).
9. M. S. Vitiello, G. Scamarcio, V. Spagnolo, B. S. Williams, S. Kumar, Q. Hu, and J. L. Reno, "Measurement of subband electronic temperatures and population inversion in THz quantum-cascade lasers," Appl. Phys. Lett. 86, 111115 (2005).
10. J. T. Lu and J. C. Cao, Appl. Phys. Lett. "Monte Carlo simulation of hot phonon effects in resonant-phonon-assisted terahertz quantum-cascade lasers," 88, 061119 (2006).
11. C. Sirtori, F. Capasso, J. Faist, A. L. Hutchinson, D. L. Sivco, and A. Y. Cho, "Resonant tunneling in quantum cascade lasers," IEEE J. Quantum Electron. 34, 1722 (1998).
12. S. Kohen, B. S. Williams, and Q. Hu, "Electromagnetic modeling of terahertz quantum cascade laser waveguides and resonators," J. Appl. Phys. 97, 053106 (2005).
13. L. Ajili, G. Scalari, J. Faist, H. Beere, E. Linfield, D. Ritchie, and G. Davies, "High power quantum cascade lasers operating at $\lambda \sim 87$ and 130 μm," Appl. Phys. Lett., 85, 3986 (2004).
14. J. Alton, et al.: 'Optimum resonant tunneling injection and influence of doping density on the performance of THz bound-to-continuum cascade lasers', Proc. SPIE 5727, 65–73 (2005).
15. B. S. Williams, S. Kumar, Q. Hu, and J. L. Reno, "High-power terahertz quantum-cascade lasers," Electron. Lett. 42, 89 (2006).
16. Williams, B.S., H. C. Callebaut, S. Kumar, Q. Hu and J. L. Reno, "3.4-THz quantum cascade laser based on longitudinal-optical-phonon scattering for depopulation," Appl. Phys. Lett., 82, 1015 (2003).
17. A. W. M. Lee, B. S. Williams, S. Kumar, Q. Hu, and J. L. Reno, "Real-time imaging using a 4.3 THz quantum cascade laser and a 320x240 microbolometer focal-plane array," IEEE Photonics Technol. Lett. **18**, 1415 (2006).
18. A. W. M. Lee, Qi Qin, S. Kumar, B. S. Williams, Q. Hu, and J. L. Reno, "Real-time terahertz imaging over a standoff distance (>25 meters)," Appl. Phys. Lett. **89**, 141125 (2006).